Electronic Supplementary Material to: Comparison of the Anthropogenic Emission Inventory for CMIP6 Models with a Country-Level Inventory over China and the Simulations of the Aerosol Properties*

Tianyi FAN[1], Xiaohong LIU[2], Chenglai WU[3], Qiang ZHANG[4],
Chuanfeng ZHAO[1], YANG Xin[1], and Yanglian LI[1]

[1]*College of Global Change and Earth System Science*, *Beijing Normal University*, *Beijing* 100875, *China*
[2]*Department of Atmospheric Sciences*, *Texas A&M University*, *College Station*, *Texas* 77843, *USA*
[3]*International Center for Climate and Environment Sciences*, *Institute of Atmospheric Physics*,
Chinese Academy of Sciences, *Beijing* 100029, *China*
[4]*Department of Earth System Science*, *Tsinghua University*, *Beijing* 100091, *China*

ESM to: Fan, T. Y., X. H. Liu, C. L. Wu, Q. Zhang, C. F. Zhao, X. Yang, and Y. L. Li, 2022: Comparison of the anthropogenic emission inventory for CMIP6 models with a country-level inventory over China and the simulations of the aerosol properties. *Adv. Atmos. Sci.*, **39**(1), 80–96, https://doi.org/10.1007/s00376-021-1119-6.

Section S1. Geographic locations

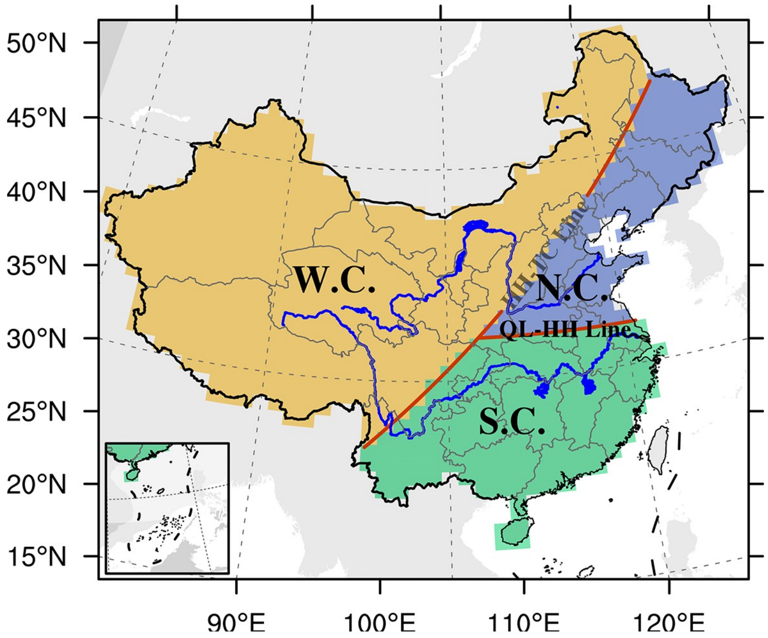

Fig. S1. Geographic locations for Northern China (NC), southern China (SC), western China (WC), the Heihe-Tengchong (HH-TC) Line, and the Qinling-Huaihe (QL-HH) Line.

---

*The online version of this article can be found at https://doi.org/10.1007/s00376-021-1119-6.

Section S2. Location- and time-dependence of the most frequent months of maximum emissions (MFMMEs)

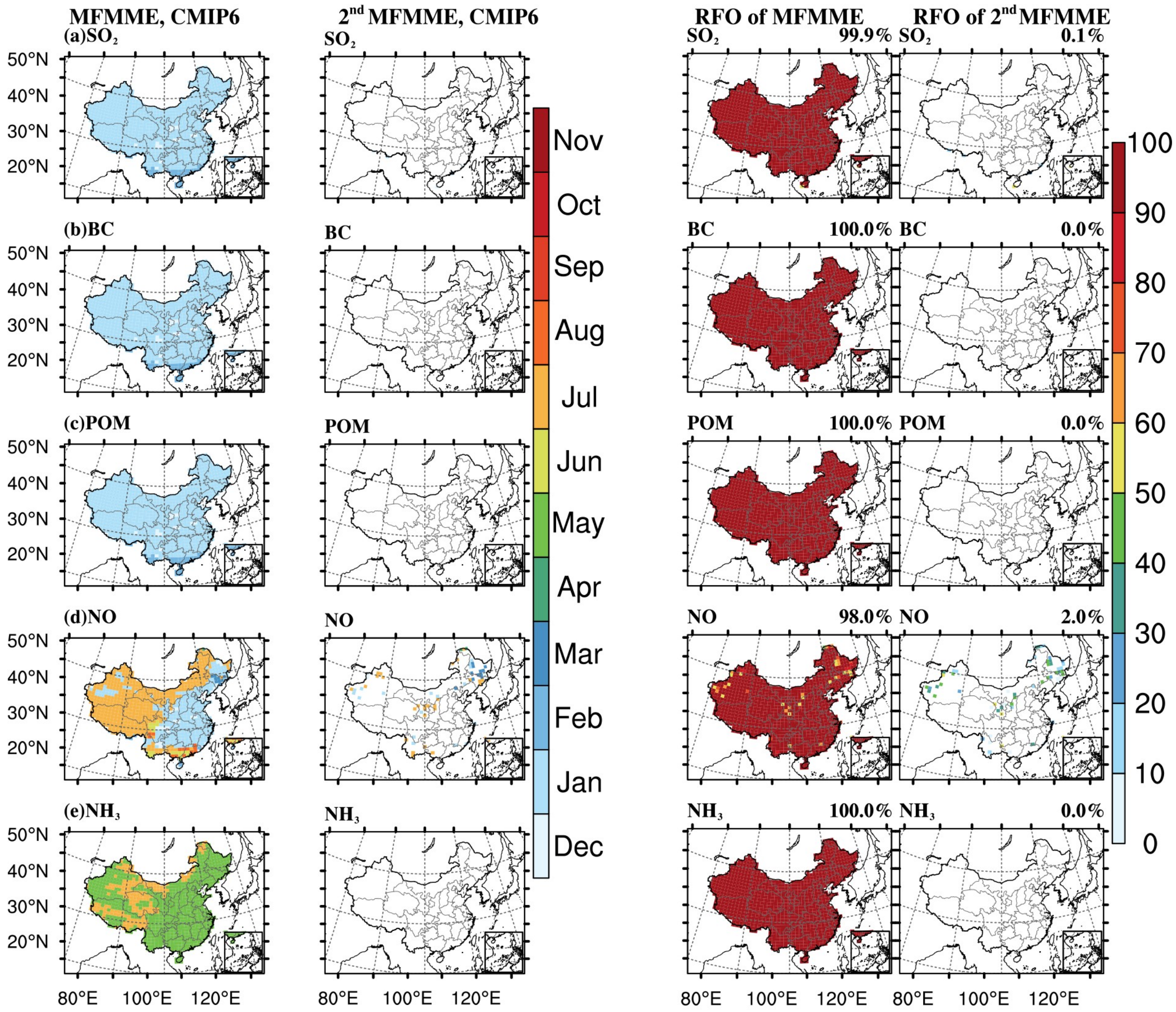

Fig. S2. The spatial distribution of the MFMMEs and second MFMMEs from 2000 to 2015 for (a) SO_2, (b)BC, (c)POM, (d)NO, and (e) NH_3 in the CMIP6 emission inventory. The relative frequency of occurrence (RFO) of MFMMEs and second MFMMEs are also shown for these species. We obtain the MFMME and second MFMME by sorting the frequency of months with maximum emission rates in the year from high to low during the 16 years and define the months with most and second most frequencies of occurrence as MFMME and second MFMME, respectively. RFOs for MFMME and second MFMME are calculated by dividing the numbers of years when MFMME and second MFMME occurred, respectively, by 16 years (2000–2015). The percentage numbers in the RFO plots are the country-wide averaged RFOs.

Section S3. Evaluating the AOD bias over China

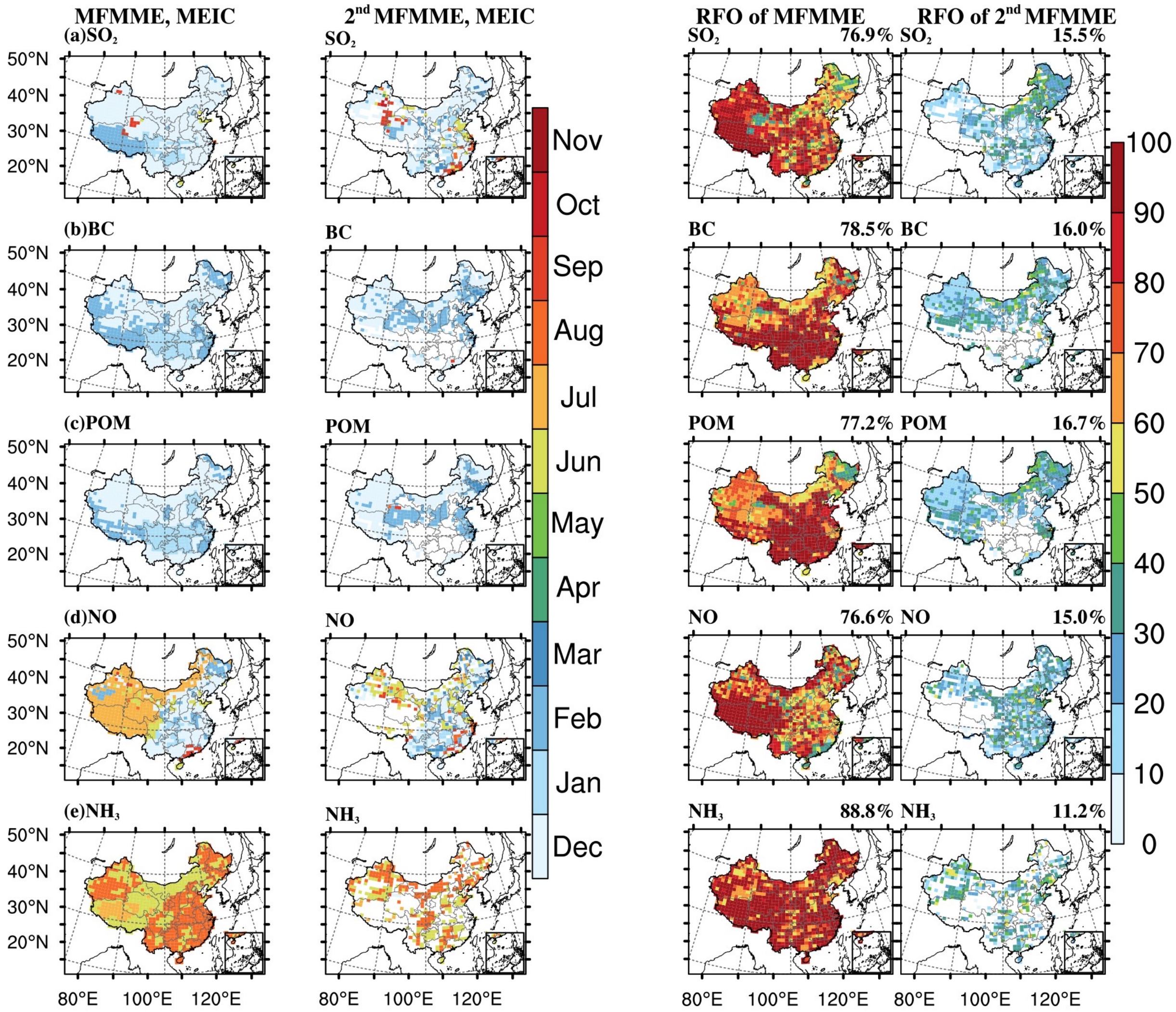

Fig. S3. Same as Fig. S2, but for the MEIC emission inventory.

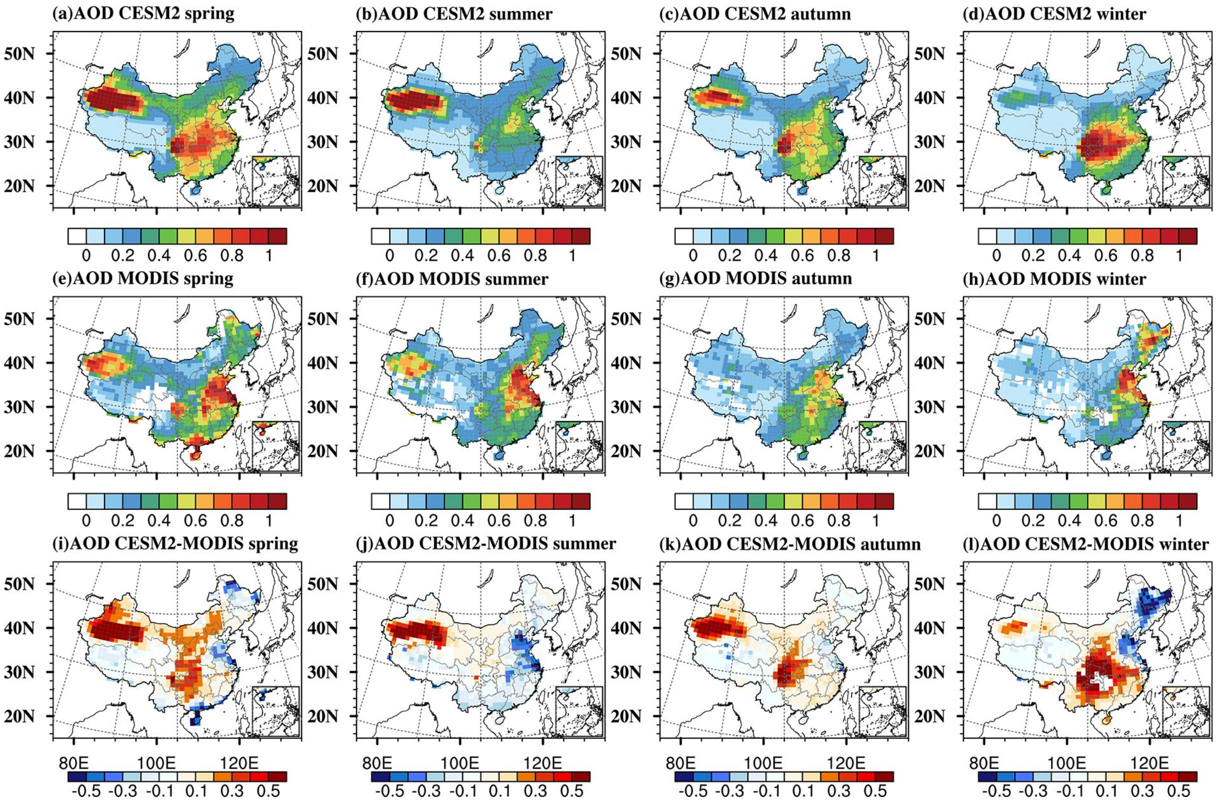

Fig. S4. Spatial distribution of CESM2 simulated AOD using CMIP6 emission inventory in (a) spring (March, April, and May), (b) summer (June, July, and August), (c) autumn (September, October, and November), and (d) winter (December, January, and February), MODIS retrieved AOD in the each season (e)–(h), and the difference between CESM2 and MODIS AOD in each season (i)–(l) for the year 2015.

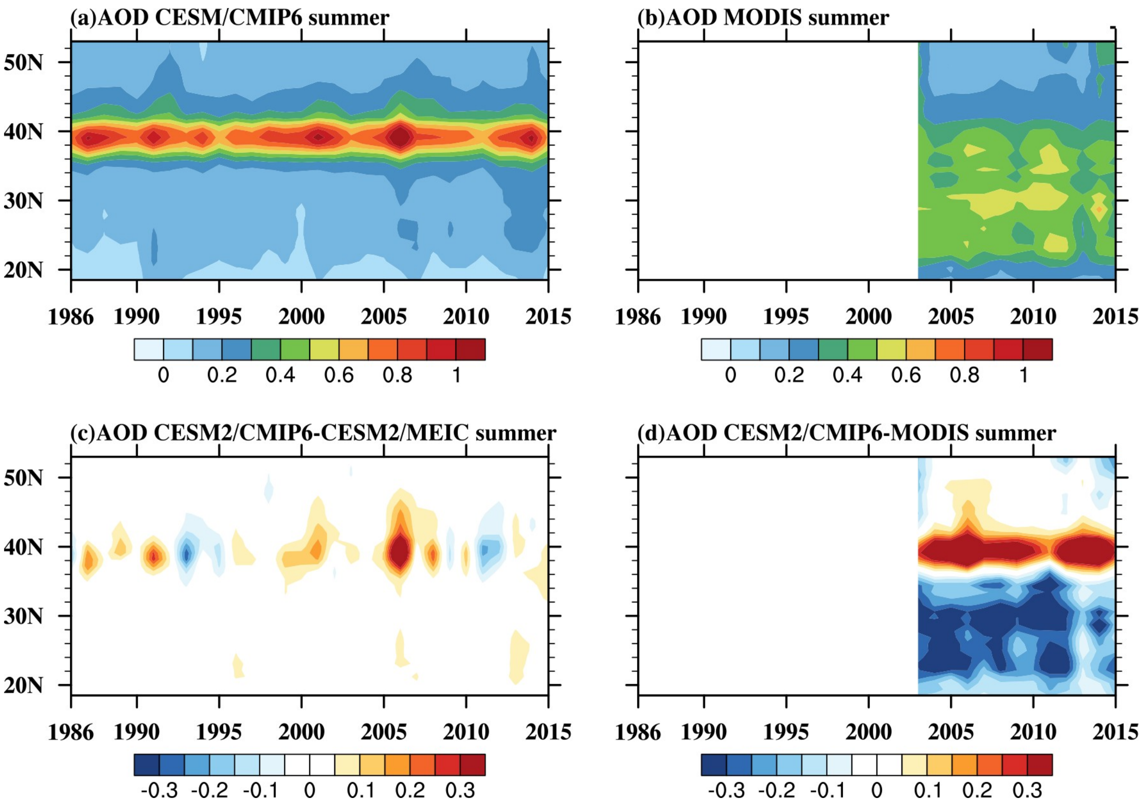

Fig. S5. Time evolution of the latitudinal averages of AODs in summer (June, July, and August) for (a) CESM2 simulation with CMIP6 emissions from 1986 to 2015, (b) MODIS retrievals from 2002 to 2015, (c) the difference between CESM2 simulation with CMIP6 and MEIC emissions, and (d) the difference between CESM2/CMIP6 simulation and the MODIS retrievals. The overestimation of AOD around 40°N is mainly over the Taklamakan Desert in western China, which is partly offset by the underestimation in northern China (see Fig. S4). The underestimation south of 40°N is mainly due to bias in southern China. The model biases are persistent in the summer over all the years.

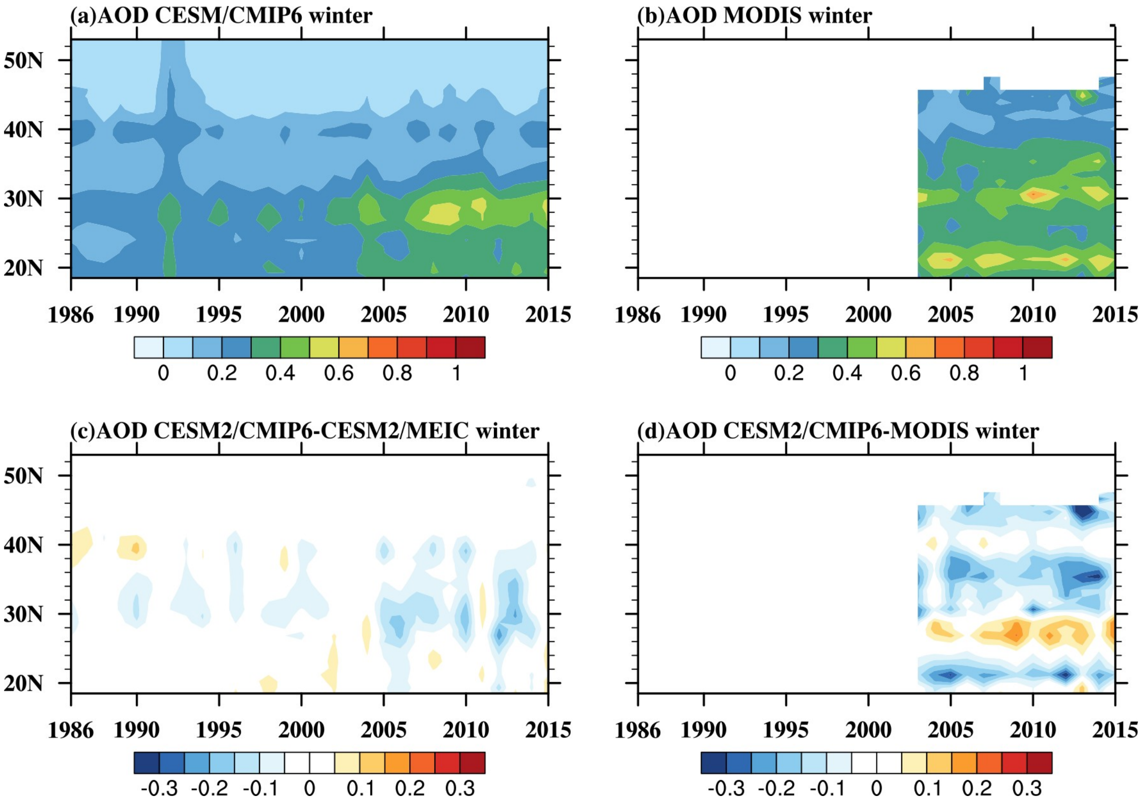

Fig. S6. Same as Fig. S5, but for winter (December, January, and February). The overestimation between 24°N and 30°N is mainly due to the high bias over Sichuan Basin (see Fig. S4). The underestimation between 30°N and 40°N is mainly due to the low bias over NCP, which is partly offset by the high bias over Sichuan Basin. The underestimation north of 40°N comes from northeastern China. The model biases are persistent over all the years.

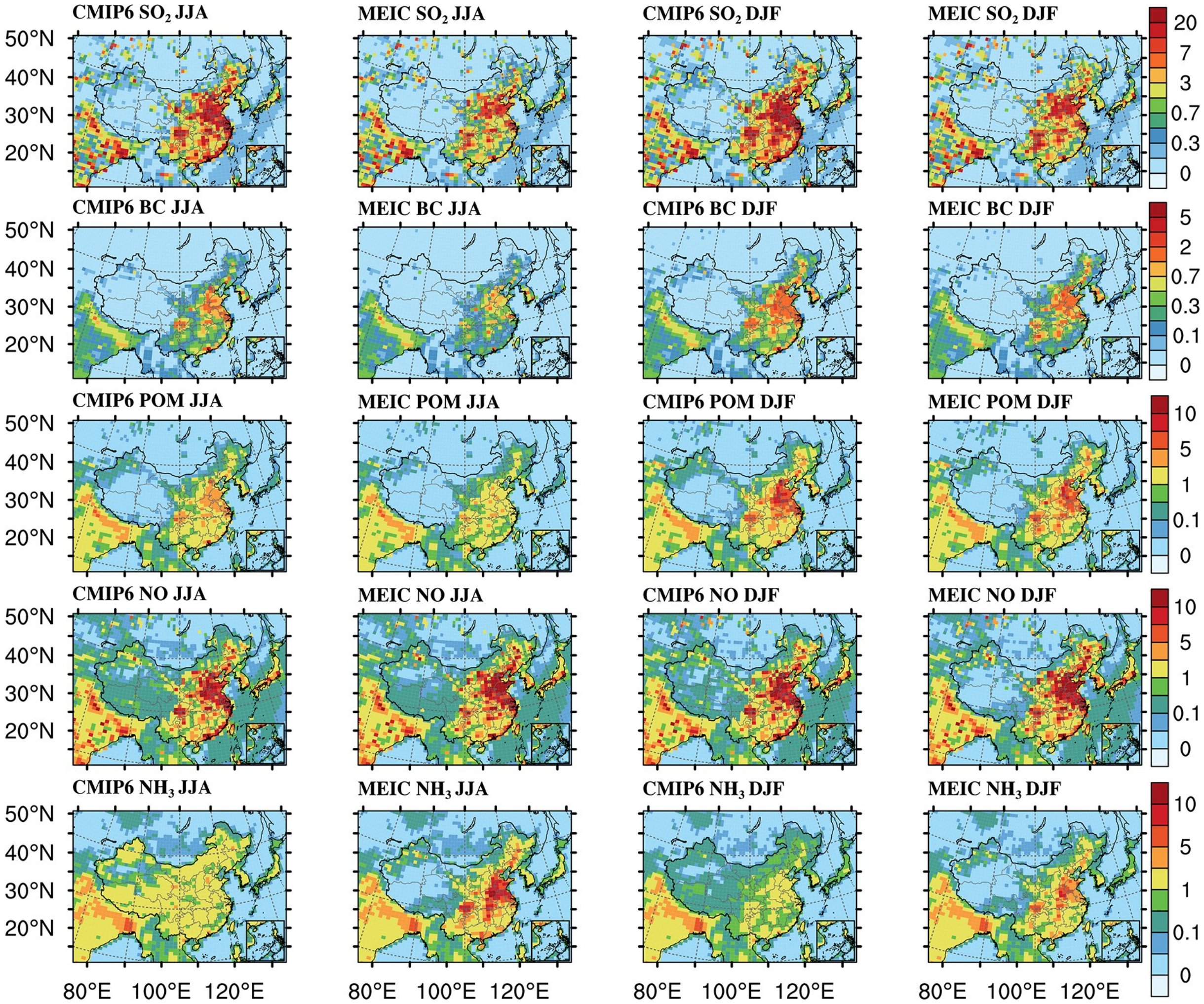

Fig. S7. Spatial distribution of emission rates (units: g m^{-2} yr^{-1}) of SO_2, BC, POM, NO, and NH_3 in the CMIP6 and MEIC inventories in summer (June, July, and August, JJA) and winter (December, January, and February, DJF) of the year 2015.

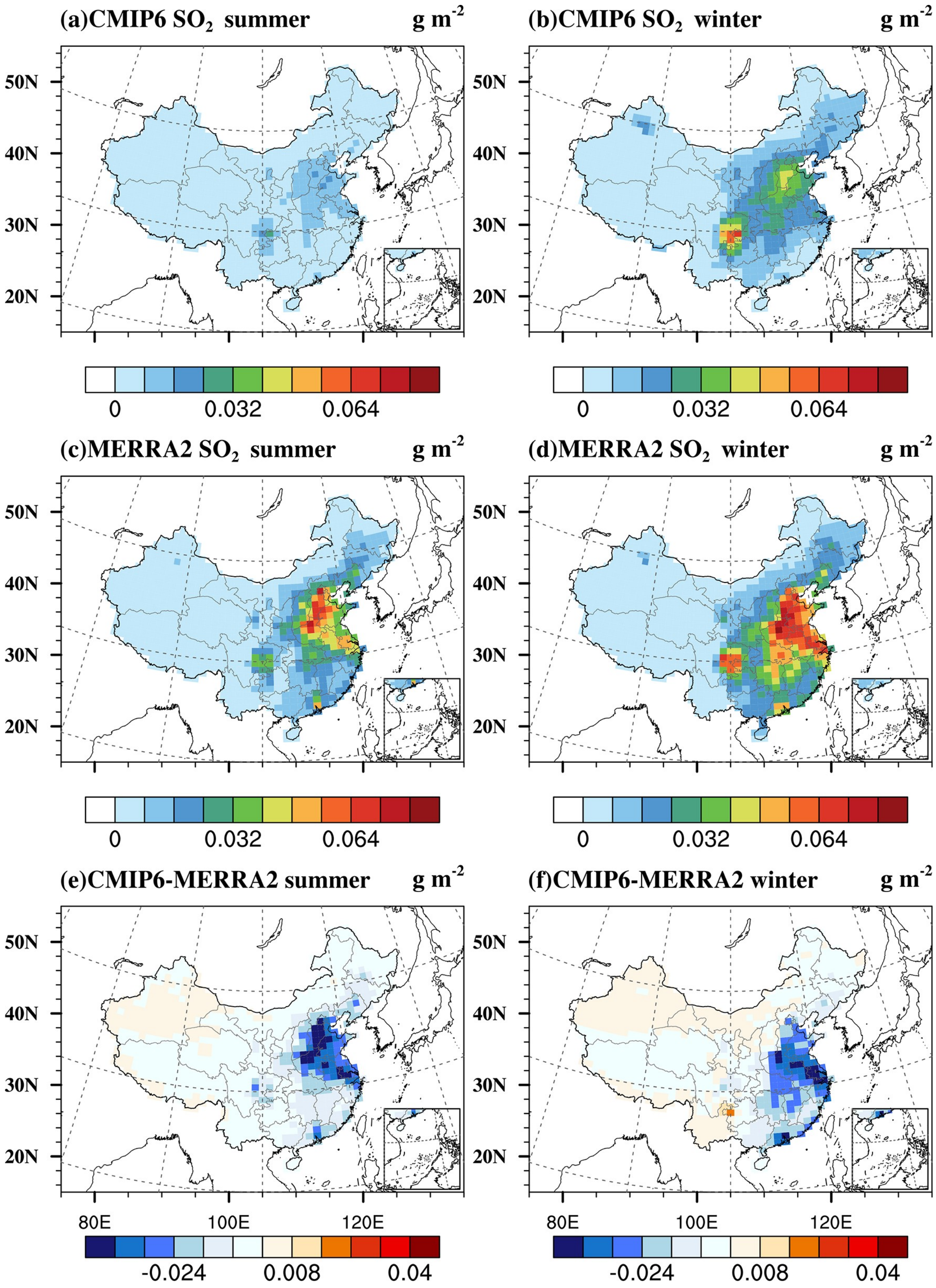

Fig. S8. Spatial distribution of column integrated SO$_2$ mass (units: g m^{-2}) simulated by CESM2 with the CMIP6 emission inventory (a) in summer (June, July, and August) and (b) in winter (December, January, and February), MERRA-2 SO$_2$ (c) in summer and (d) in winter, and the difference between CESM2 and MERRA-2 (e) in summer and (f) in winter for the year 2015.

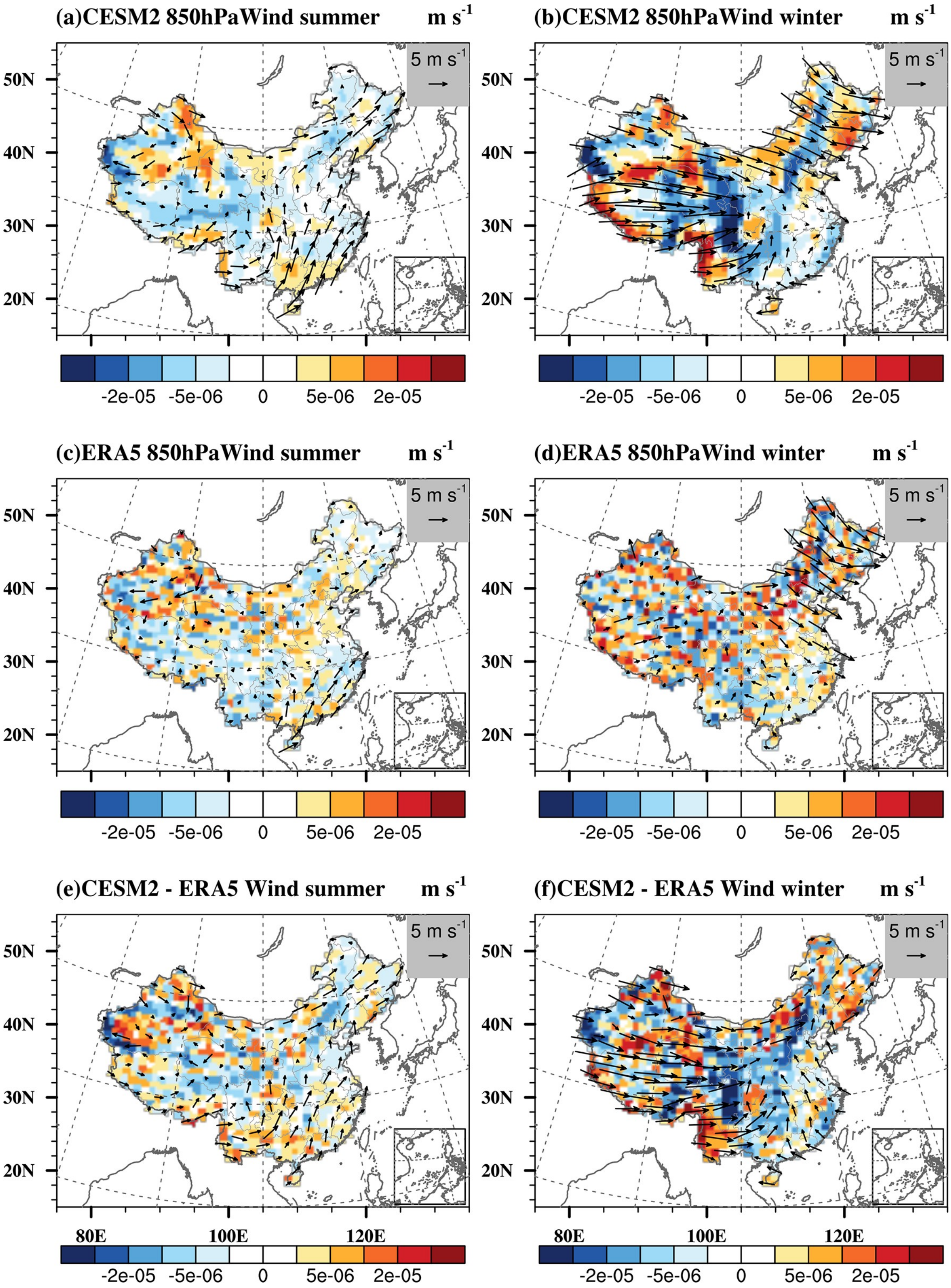

Fig. S9. Same as Fig. S8, but for CESM2 simulated wind (units: m s^{-1}) compared with ERA5 reanalysis at the 850-hPa pressure level for the year 2015. The filled colors represent the divergence of the wind field ($\nabla \cdot U$). Positive values mean divergence and negative values mean convergence.

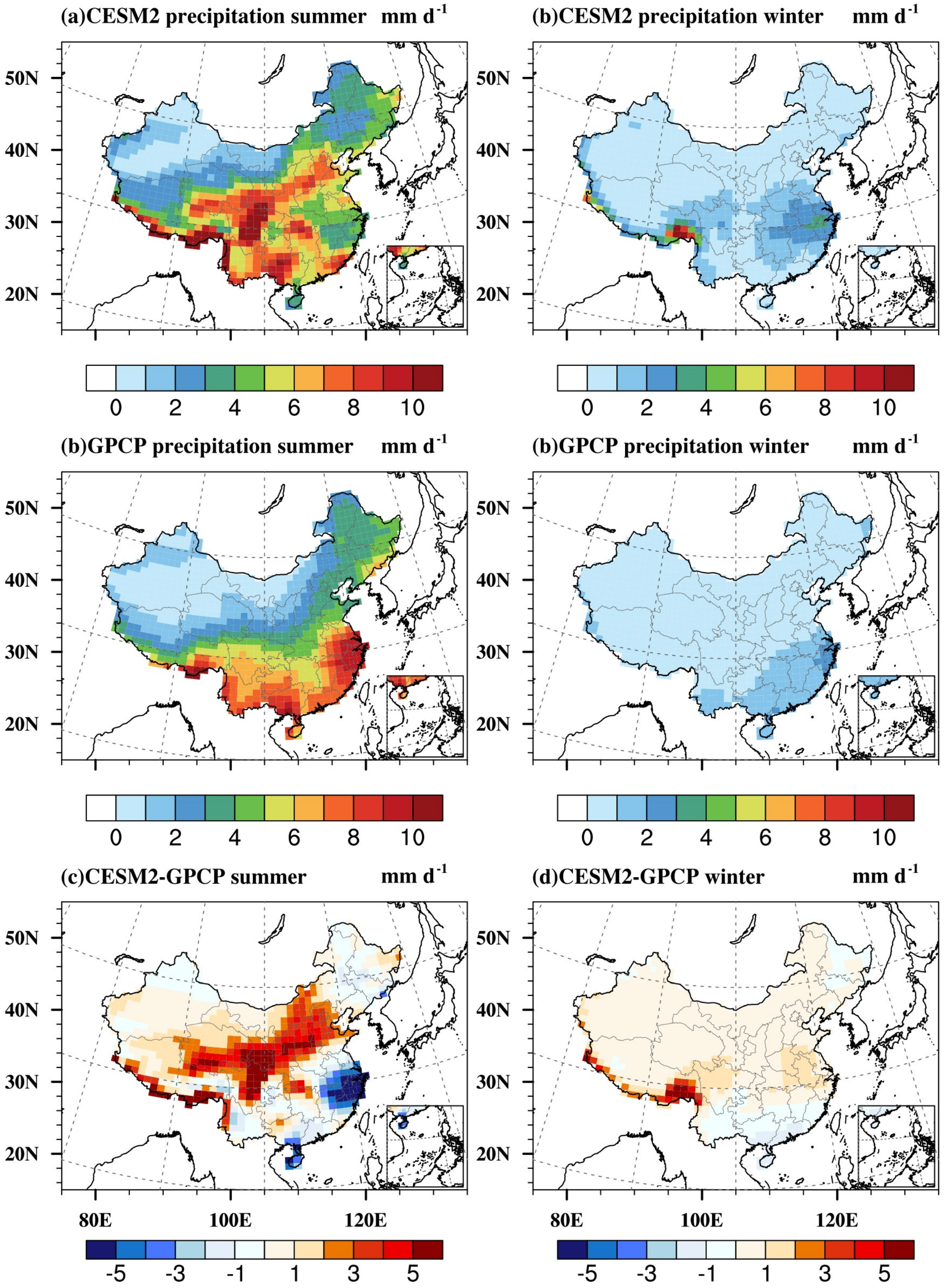

Fig. S10. Same as Fig. S8, but for precipitation rates (units: mm d^{-1}) simulated by CESM2 compared with GPCP observation for the year 2015.

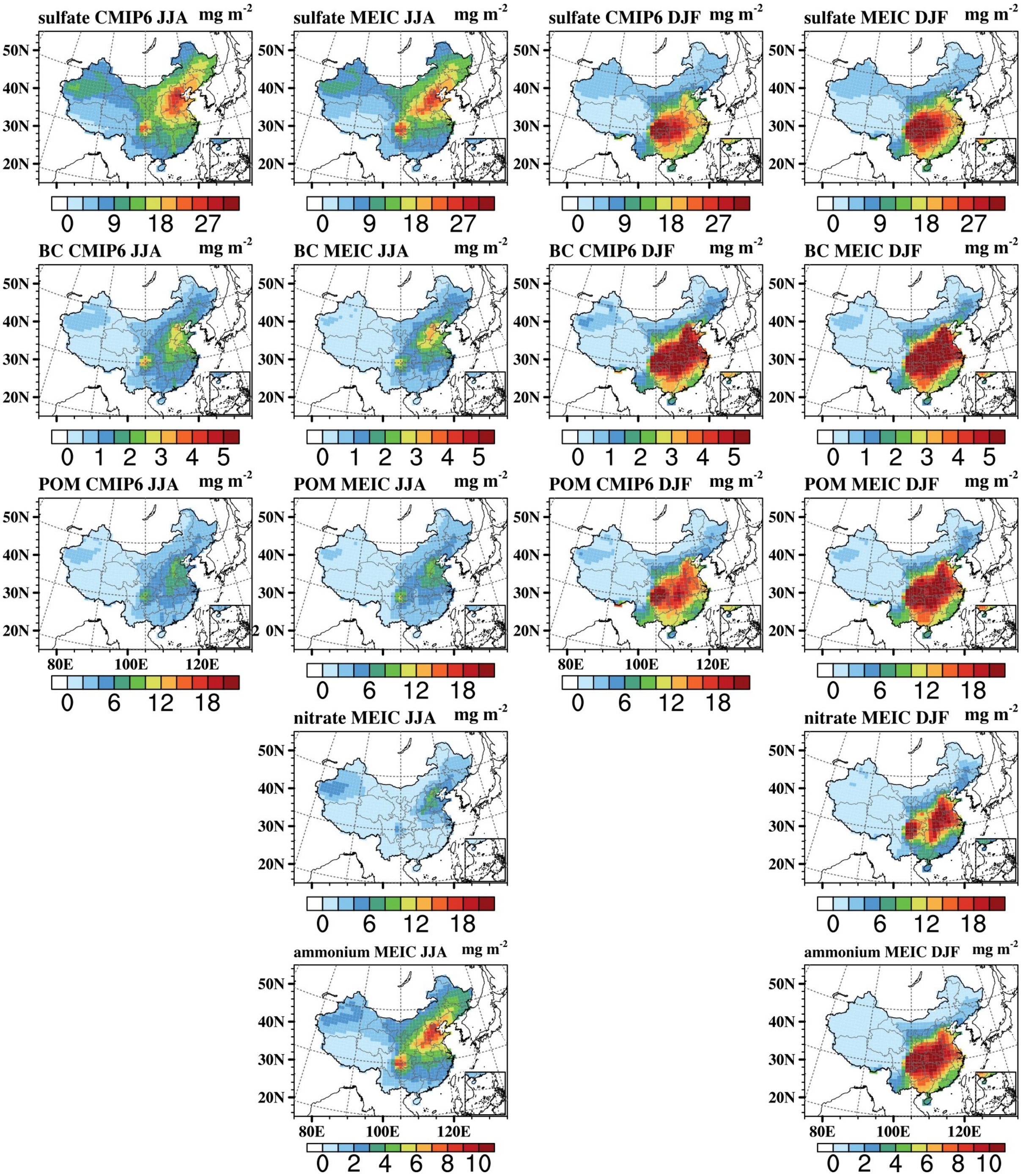

Fig. S11. Spatial distribution of sulfate, BC, POM, nitrate, and ammonium aerosols (units: mg m^{-2}) simulated by CESM2 with MEIC and CMIP6 emissions in the summer (June, July, and August, JJA) and in the winter (December, January, and February, DJF) of the year 2015.

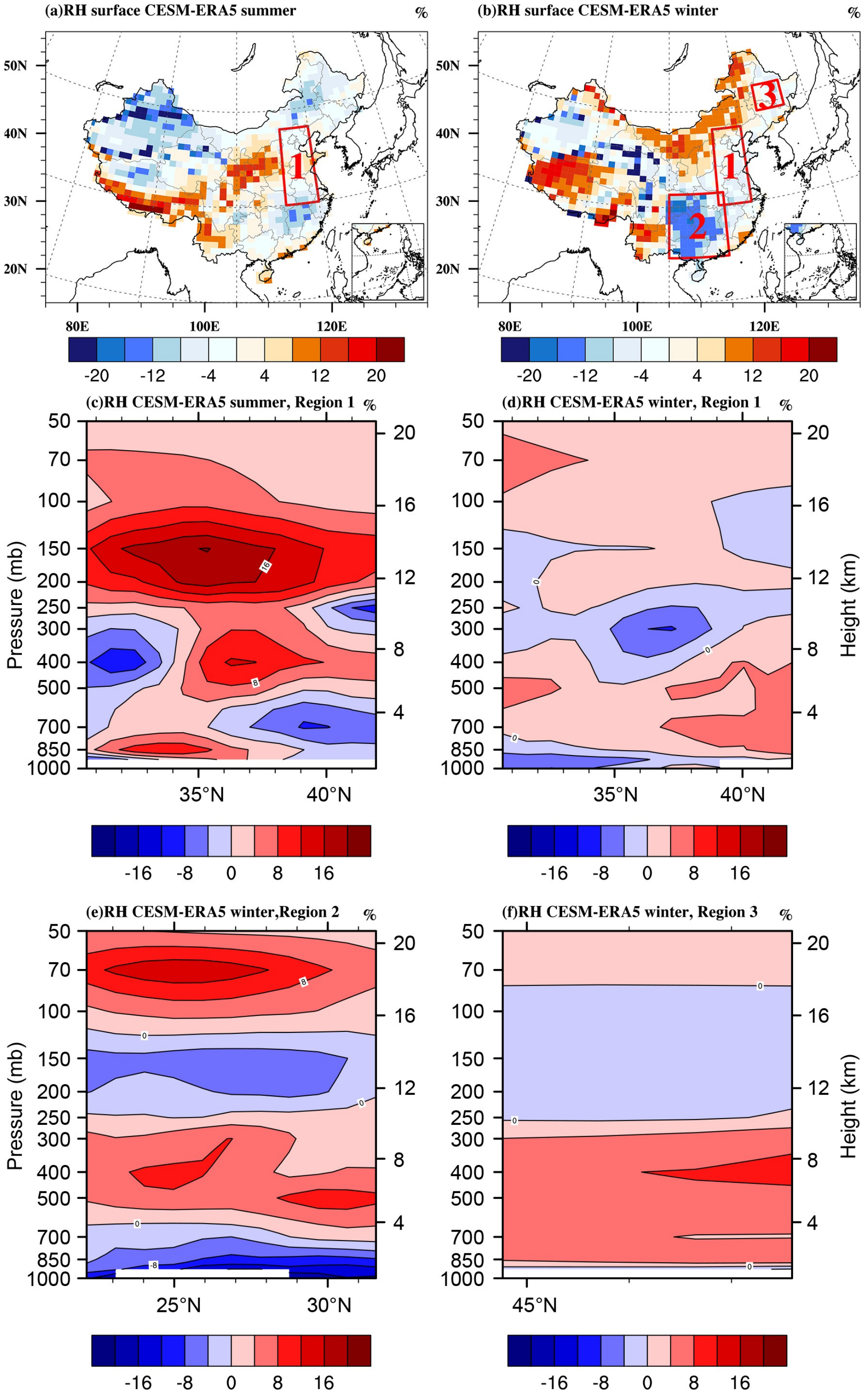

Fig. S12. Spatial distribution of the difference of relative humidity (RH) between CESM2 and ERA5 reanalysis at the surface in (a) summer and (b) winter; Regions 1, 2, and 3 where the AODs are most biased are located with red rectangles. Vertical profiles of the RH differences between CESM2 and ERA5 in (c) Region 1 in summer, (d) Region 1 in winter, (e) Region 2 in winter, and (f) Region 3 in winter. The vertical profiles are longitudinally averaged over the regions, where Regions 1 represents northern China (30°–42°E, 114°–120°E), Region 2 represents southwestern China (22°–32°E, 105°–115°E), and Region 3 represents northeastern China (44°–48°E, 124°–130°E).

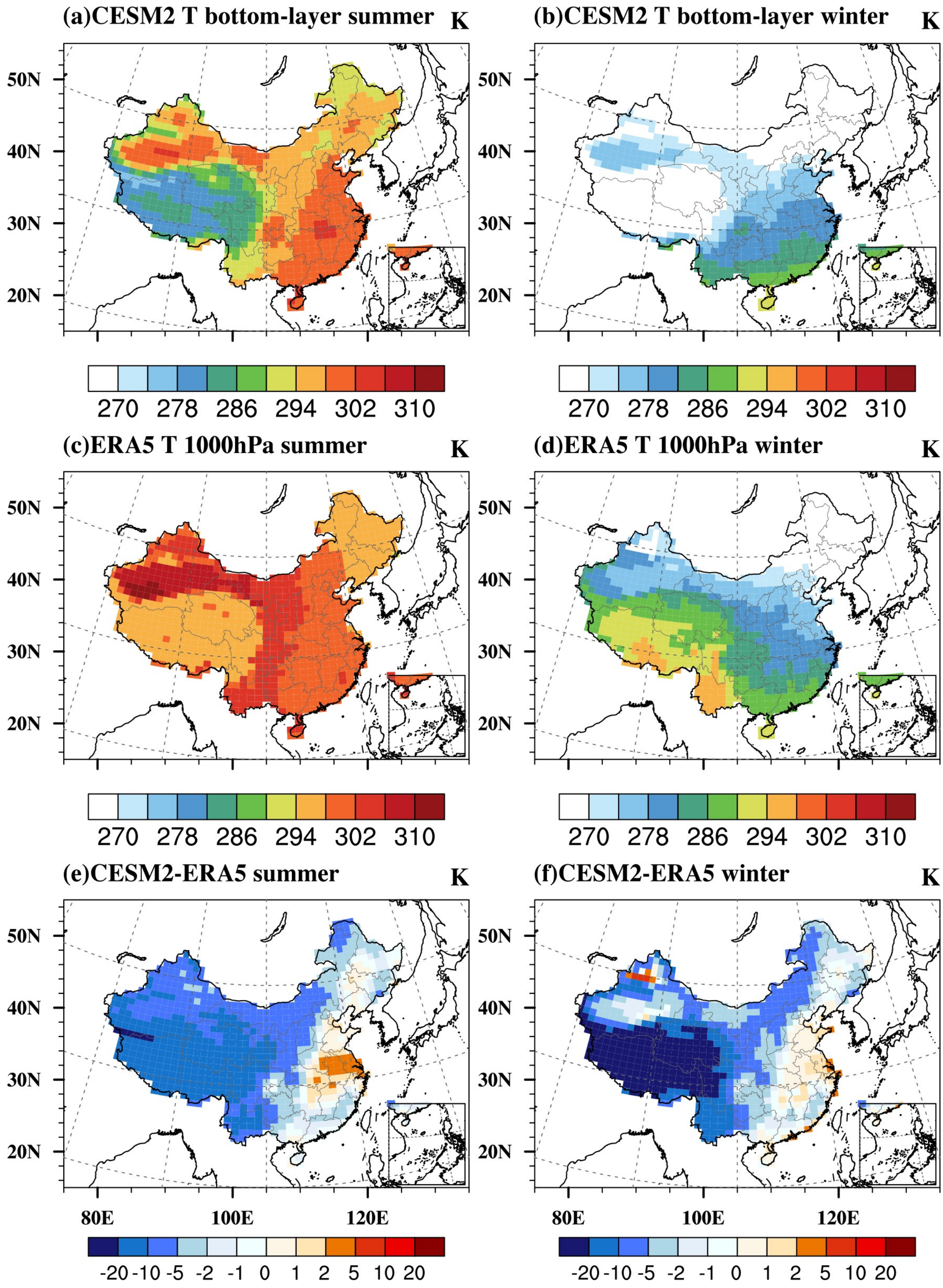

Fig. S13. Same as Fig. S8, but for temperature (units: K) at the lowest model layer for CESM2 results or 1000 hPa for ERA5 reanalysis.

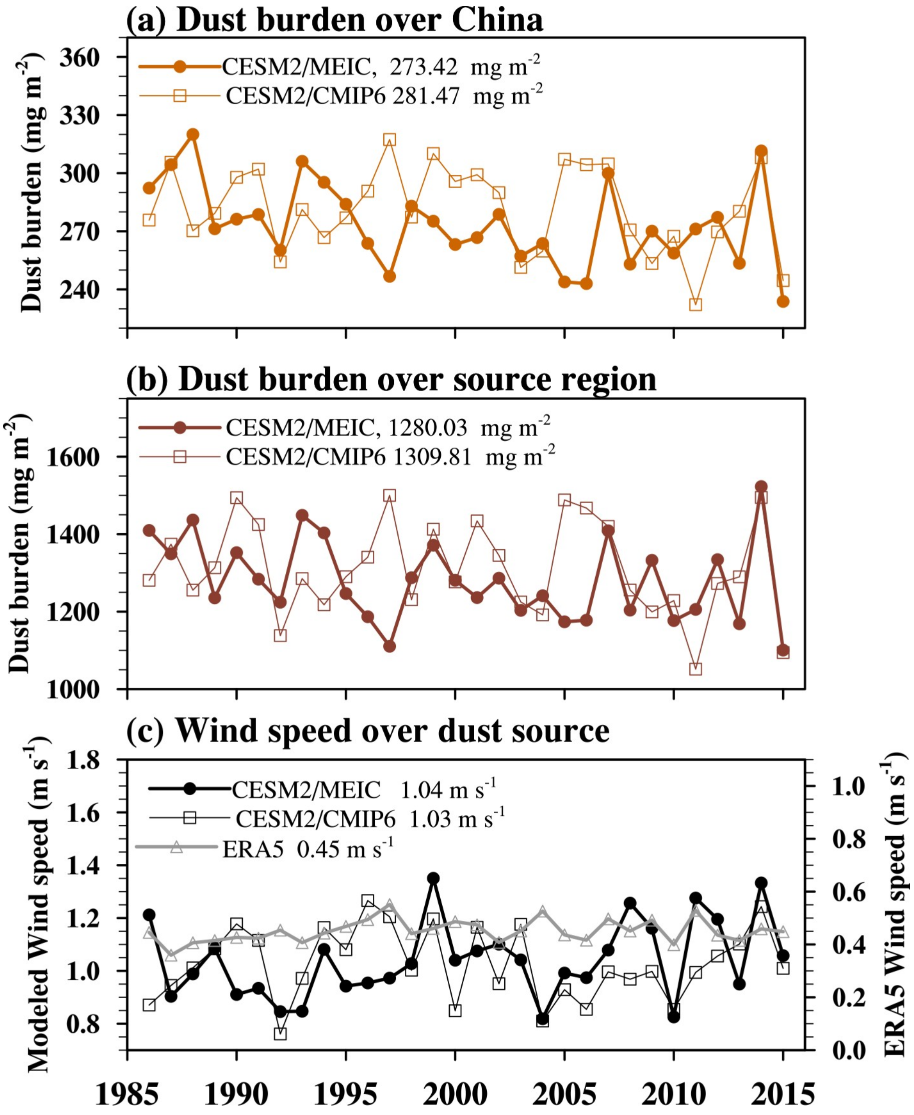

Fig. S14. Yearly trends of the simulated dust burdens (units: mg m^{-2}) by CESM2 using CMIP6 and MEIC emission inventories during 1986–2015 (a) averaged over China and (b) over the source region (36°–42°N, 75°–95°E). (c) Yearly trends of the surface wind speeds averaged over the source regions by the CESM2 simulations and the ERA5 reanalysis dataset. The numbers in the legend are averaged dust burdens for (a) and (b) and wind speed for (c) over 1986–2015.

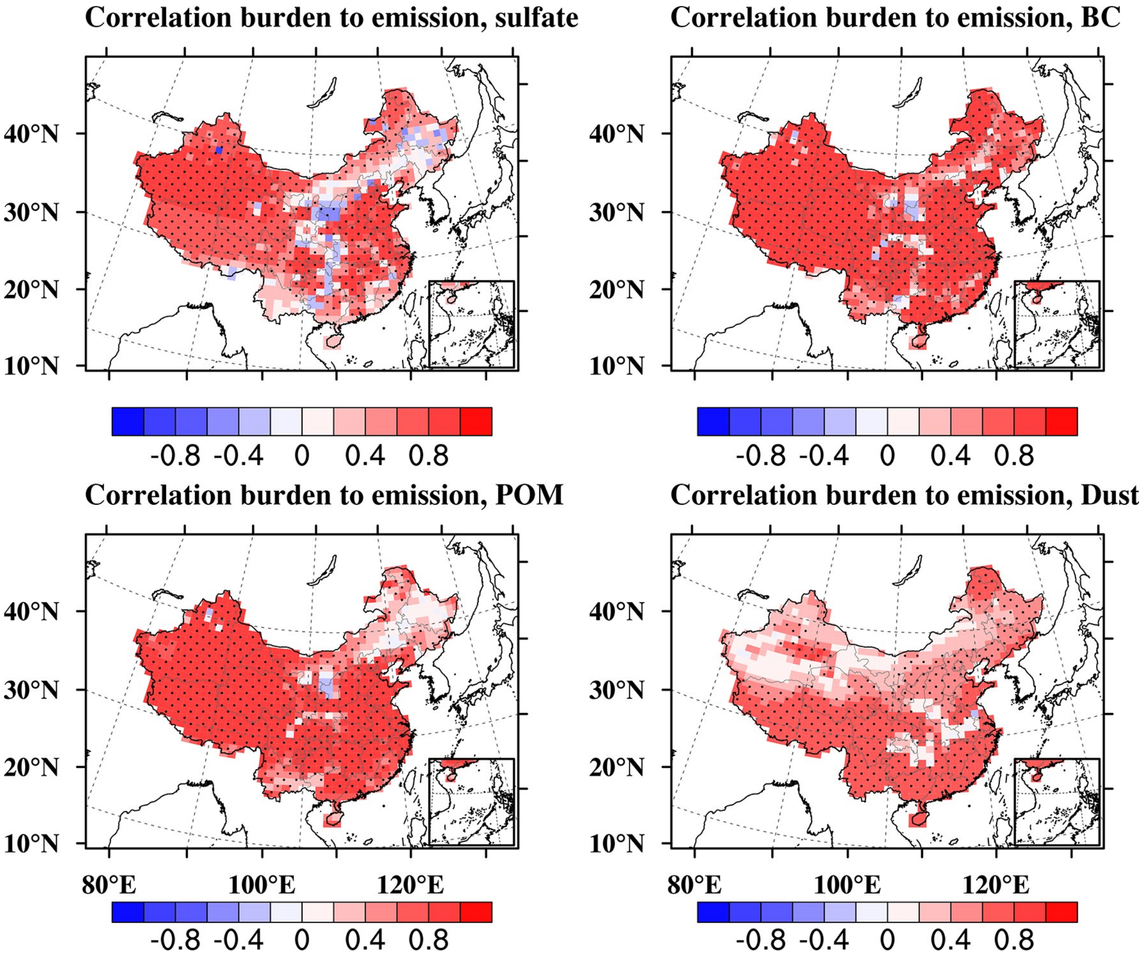

Fig. S15. Spatial distribution of correlation of the aerosol burden change to the emission perturbation between the CMIP6 and MEIC runs for (a) sulfate, (b) BC, (c) POM, and (d) dust.

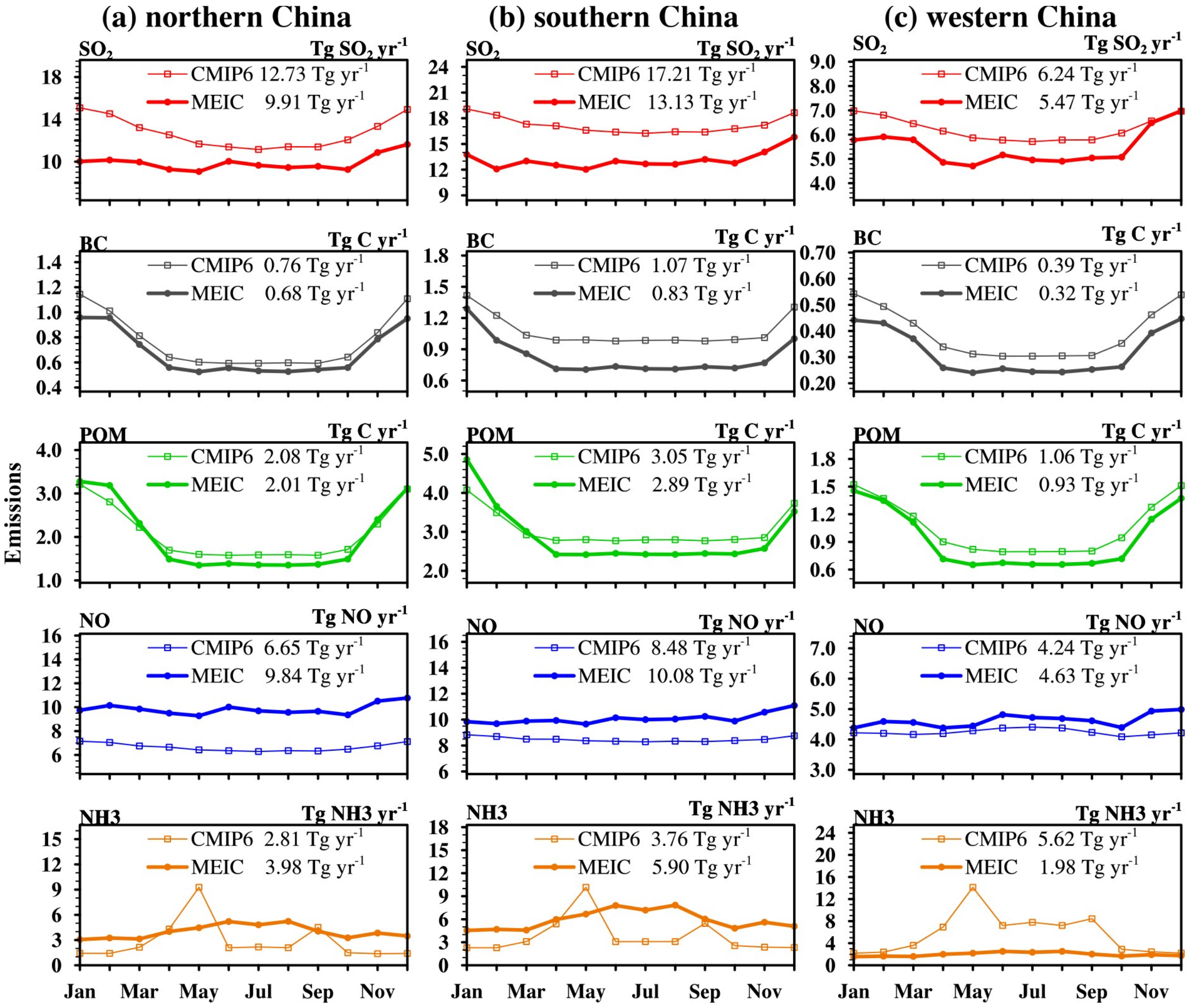

Fig. S16. Seasonal variations of the emission of various species in column (units: Tg yr^{-1}) (a) northern China, column (b) southern China, and column (c) western China.

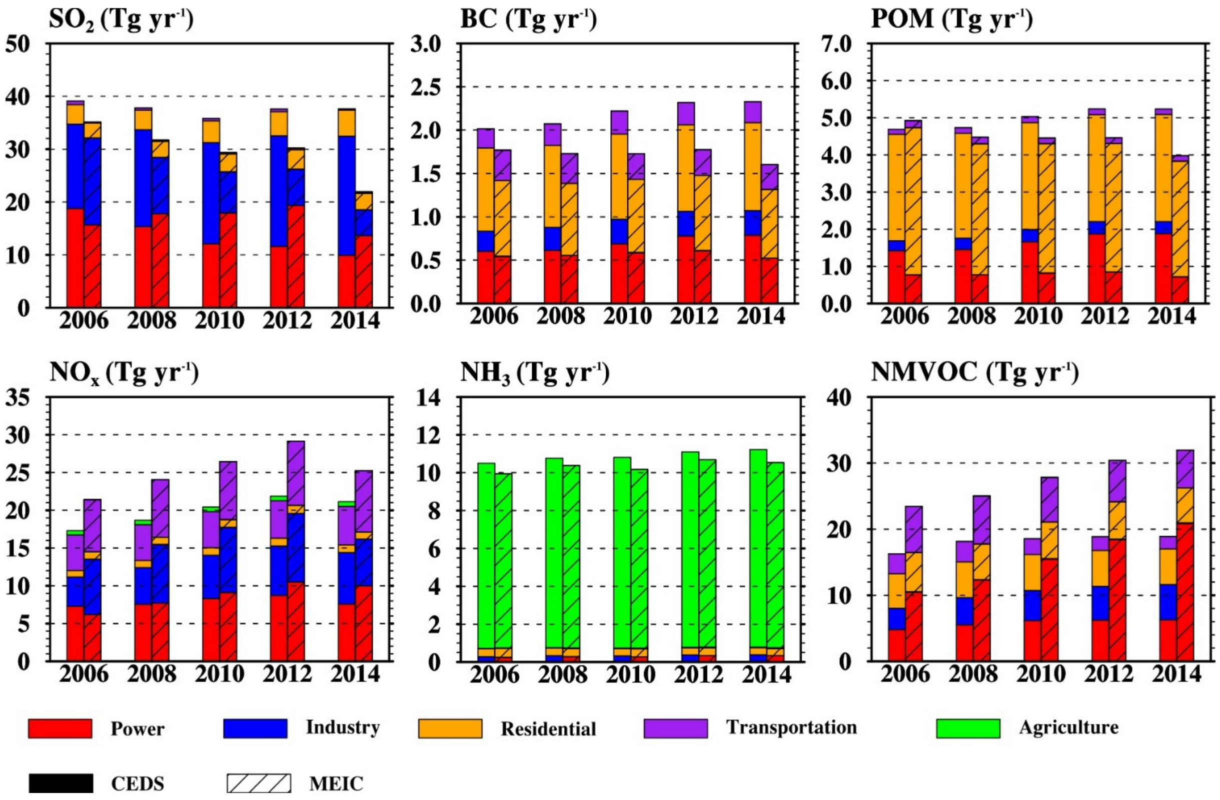

Fig. S17. Comparison of the CMIP6 (CEDS) and MEIC emission rates (units: Tg yr^{-1}) by sectors for SO_2, BC, POM, NO_x, NH_3, and NMVOC. NMVOC speciation in the CB05 chemical mechanism provided by MEIC (Li et al., 2014). Here, the total NMVOC emission rate in MEIC is obtained by adding up all the NMVOC species. Total NMVOC emission rate in CMIP6 is provided by CEDS.

REFERENCES

Li, M., and Coauthors, 2014: Mapping Asian anthropogenic emissions of non-methane volatile organic compounds to multiple chemical mechanisms. *Atmospheric Chemistry and Physics*, **14**, 5617–5638, https://doi.org/10.5194/acp-14-5617-2014.